American Mineralogist, Volume 92, pages 1383–1394, 2007

Characterization of mineral surfaces using FIB and TEM: A case study of naturally weathered alkali feldspars

Martin R. Lee,[1,*] David J. Brown,[1,†] Caroline L. Smith,[2] Mark E. Hodson,[3] Maureen MacKenzie,[4] and Roland Hellmann[5]

[1]Department of Geographical and Earth Sciences, University of Glasgow, Gregory Building, Lilybank Gardens, Glasgow, G12 8QQ, U.K.
[2]Department of Mineralogy, Natural History Museum, Cromwell Road, London, SW7 5BD, U.K.
[3]Department of Soil Science, School of Human and Environmental Sciences, The University of Reading, Whiteknights, Reading, RG6 6DW, U.K.
[4]Department of Physics and Astronomy, University of Glasgow, Glasgow, G12 8QQ, U.K.
[5]Environmental Geochemistry Group, LGIT, CNRS UMR 5559-OSUG-Université J. Fourier, France

Abstract

Using a focused ion beam (FIB) instrument, electron-transparent samples (termed foils) have been cut from the naturally weathered surfaces of perthitic alkali feldspars recovered from soils overlying the Shap granite, northwest England. Characterization of these foils by transmission electron microscopy (TEM) has enabled determination of the crystallinity and chemical composition of near-surface regions of the feldspar and an assessment of the influence of intragranular microtextures on the microtopography of grain surfaces and development of etch pits. Damage accompanying implantation of the 30 kV Ga^+ ions used for imaging and deposition of protective platinum prior to ion milling creates amorphous layers beneath outer grain surfaces, but can be overcome by coating grains with >85 nm of gold before FIB work. The sidewalls of the foil and feldspar surrounding original voids are also partially amorphized during later stages of ion milling.

No evidence was found for the presence of amorphous or crystalline weathering products or amorphous "leached layers" immediately beneath outer grain surfaces. The absence of a leached layer indicates that chemical weathering of feldspar in the Shap soils is stoichiometric, or if non-stoichiometric, either the layer is too thin to resolve by the TEM techniques used (i.e., ≤~2.5 nm) or an insufficient proportion of ions have been leached from near-surface regions so that feldspar crystallinity is maintained. No evidence was found for any difference in the mechanisms of weathering where a microbial filament rests on the feldspar surface. Sub-micrometer-sized steps on the grain surface have formed where subgrains and exsolution lamellae have influenced the propagation of fractures during physical weathering, whereas finer scale corrugations form due to compositional or strain-related differences in dissolution rates of albite platelets and enclosing tweed orthoclase. With progressive weathering, etch pits that initiated at the grain surface extend into grain interiors as etch tubes by exploiting preexisting networks of nanopores that formed during the igneous history of the grain. The combination of FIB and TEM techniques is an especially powerful way of exploring mechanisms of weathering within the "internal zone" beneath outer grain surfaces, but results must be interpreted with caution owing to the ease with which artifacts can be created by the high-energy ion and electron beams used in the preparation and characterization of the foils.

Keywords: FIB, TEM, alkali feldspar, weathering

Introduction

The focused ion beam (FIB) instrument has been used extensively by materials scientists to prepare electron-transparent specimens of synthetic materials for imaging and chemical analysis at high spatial resolutions by transmission electron microscopy (TEM) (e.g., Anderson et al. 1992), and it is also now being applied to the Earth and planetary sciences (e.g., Stroud et al. 2000; Heaney et al. 2001; Lee et al. 2003; Wirth 2004). The objective of most of this work has been to characterize the bulk properties of the material and very few studies have utilized the considerable advantages of the FIB technique over conventional Ar^+ ion milling for manufacturing cross sections of the surfaces and near-surface regions of mineral grains. Weathering is one field where these techniques could provide many new insights because the surfaces of grains from soils are typically pitted and partly or completely obscured by debris and reaction products. The FIB can be used to make cross sections of such irregular and coated grains to enable characterization by

* E-mail: Martin.Lee@ges.gla.ac.uk
† Present address: Department of Civil and Structural Engineering, University of Sheffield, Kroto Research Institute, Broad Lane, Sheffield, S3 7HQ, U.K.

0003-004X/07/0809–1383$05.00/DOI: 10.2138/am.2007.2453

TEM of reaction products, the outermost grain surface, and the unmodified interior of the mineral, thereby providing a new and very powerful method for studying weathering mechanisms. For example, the influence of intragranular microtextures on weathering rates at the grain surface can be explored by examining the cross-sectional morphology of etch pits and the properties of the surrounding crystal structure. The chemistry of weathering, in particular reaction stoichiometry, may also be investigated by characterizing any weathering products and determining whether an amorphous "leached layer" is present immediately beneath etched grain surfaces (e.g., Hellmann et al. 2003). The size and interconnectivity of pores within aggregates of reaction products and also within the weathered interiors of grains is also a very important determinant of mechanisms and rates of exchange of ions between aqueous fluids and grain surfaces (Hochella and Banfield 1995; Hochella 2002); to date this nanoscale "internal zone" has been difficult to characterize, but the FIB and TEM techniques in combination may be ideal.

The only previous combined FIB and TEM study of natural weathering was by Benzerara et al. (2005a, 2005b), who examined an orthopyroxene (OPX) grain exposed on the surface of a meteorite recovered from the Sahara. They showed that the grain was encrusted by carbonates and also found good evidence for weathering of the OPX beneath a microbial filament. As FIB and TEM in combination clearly have considerable potential in weathering research, we have sought to assess their capabilities by manufacturing and characterizing cross-sections of the surfaces and near-surface regions of naturally weathered alkali feldspars from the Shap granite, north-west England. These minerals are especially suitable for such work because the perthite microtextures of fresh and unweathered Shap feldspars have been studied in detail by TEM (Lee et al. 1995; Fitz Gerald et al. 2006), and such microtextures have been shown to strongly influence the development of etch pits on grain surfaces during laboratory etching (Wilson and McHardy 1980; Waldron et al. 1994), natural weathering (Lee and Parsons 1995; Lee et al. 1998), and diagenesis (Lee and Parsons 1998; Parsons et al. 2005). Parsons et al. (1998) and Smith et al. (1998a, 1998b, 1999) hypothesized that if alkali feldspars weathered in a similar manner during the Hadean and Archaean, the etch-pit network would have provided an ideal environment for the encapsulation and assembly of self-replicating organic molecules, which could have provided conditions conducive to the origin of life. A key requirement of this hypothesis is that the etch pits had silica-rich and organophilic walls as a consequence of non-stoichiometric dissolution during weathering, and such "leached layers" are commonly inferred to develop immediately beneath the outer surfaces of alkali feldspars and other silicates used in laboratory experiments designed to mimic natural chemical weathering (e.g., Petrović et al. 1976). However, the crystal structure of the outermost surfaces of weathered Shap feldspars has yet to be characterized and there is no consensus in the literature on whether such layers can form naturally. This study explores the potential of using the FIB to manufacture electron-transparent cross-sections of carefully selected regions of naturally weathered grain surfaces and so to provide a link between SEM-scale observations of grain surfaces and higher-resolution imaging and chemical analysis of near-surface regions by TEM.

Materials

For this study we have used alkali feldspars (bulk composition ~$Or_{70.2}Ab_{29.1}An_{0.9}$, Lee and Parsons 1997) from the Shap granite, which crops out in Cumbria, northwest England. The microtextures of these feldspars, which have been described in detail elsewhere (Lee et al. 1995, 1998; Lee and Parsons 1997; Fitz Gerald et al. 2006), are dominated by lamellar microperthites with subordinate cryptoperthites. The morphology of albite exsolution lamellae within these microtextures is controlled by minimization of misfit strain along the interface with tweed orthoclase in the Murchison plane ~($\bar{6}$01). Albite platelets within the cryptoperthites are sufficiently small to retain coherency but in microperthites, a portion of the misfit has been accommodated by development of dislocation loops that encircle albite films in the Murchison plane. One set of loops is oriented parallel to **b** and the other lies in the **a**-**c** plane (Fitz Gerald et al. 2006). The cores of many of these dislocations have been dissolved during deuteric alteration to form pairs of <10 nm sized "nanotunnels" that straddle albite films and are commonly linked by narrow cracks termed "pull-aparts" (Fitz Gerald et al. 2006). Most of this work has used naturally weathered alkali feldspars that were hand picked from raw oligo-fibrous peats that directly overlie the granite on Shap Fell. These soils are postglacial in age (i.e., ≤~15 kyr old) and the ambient soil water has a pH of ~3.4 and is undersaturated with respect to likely weathering products (Lee et al. 1998). Fresh and unweathered alkali feldspars were also studied as controls and these grains were mechanically extracted from recently quarried granite.

Methods

Naturally weathered feldspar grain surfaces were studied initially in as close to natural state as possible using a FEI Quanta 200F field-emission environmental scanning electron microscope (ESEM) operated at an accelerating voltage of 10–15 kV and using low beam currents at Glasgow. Images of centimeter-sized samples of peat containing alkali feldspars were initially acquired within the stability field of liquid water (~1°C/690 Pa), then within the stability field of water vapor (~1 °C/630 Pa). Water filling intragranular pores in those images acquired at ~1°C/690 Pa can be recognized by differences in contrast to pores that are empty and so black in the secondary electron ESEM images. The interpretation of contrast in ESEM images of wet materials is discussed further by Donald (2003). Millimeter-sized grains of alkali feldspar were subsequently hand picked from the soil, briefly immersed in distilled water to remove the largest and most weakly adhering soil particles, then mounted on Al pin stubs and coated with a thin (<~30 nm) layer of Au using an Agar sputter coater operated at ~1 kV and using a 45 mA current and vacuum of ~5 Pa. Areas of interest on (001) grain surfaces were then identified by secondary electron imaging in the Quanta ESEM operated at high vacuum. Prior to FIB work some of the grains received another coating of Au to protect their surfaces from ion beam damage in the FIB. In addition to the naturally weathered grains, electron-transparent samples were cut from the freshly created (001) cleavage surfaces of unweathered Shap alkali feldspars that had been sputter coated with different thicknesses of Au.

Cross-sections of the weathered (001) grain surfaces were cut using the FIB along a line oriented normal to **b** and the trace of ($\bar{6}$01); the plane of each sample is therefore approximately parallel to (010) (Fig. 1). The FIB work used a single-beam FEI Strata 200TEM instrument operated at 30 kV. The milling process is described below [for images of the various stages see Heaney et al. (2001), Wirth (2004) and Smith et al. (2006)]. Hereafter, an electron-transparent sample manufactured by ion milling in the FIB is referred to as a "foil," although other terms including "lamella" and "membrane" are also in common usage. Areas of interest on the grain surface that had been identified by SEM were located in the FIB by imaging using the ion beam; care was taken to find the area quickly to minimize potential damage to the grain surface. A thin grounding layer of Pt was then deposited over the area of interest by decomposition by the Ga^+ ion beam (300 pA ion current) of an organic Pt gas injected just above the surface, then a Pt strap 15 µm long by

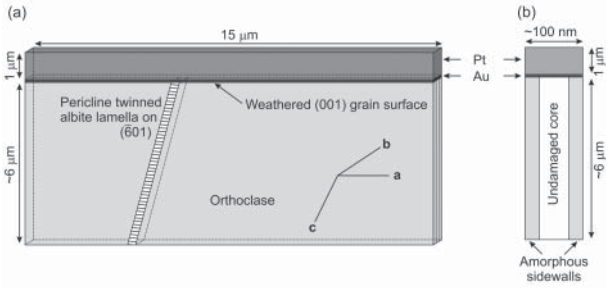

Figure 1. Diagrams illustrating the morphology, structure and orientation of the FIB-produced foils examined in this study. (**a**) A foil oriented approximately as it would be viewed in the TEM prior to tilting, but with some added perspective. The orientation of an albite exsolution lamella relative to the weathered (001) grain surface is indicated together with the three crystallographic axes of orthoclase. The layers of protective Au and Pt are also shown. (**b**) A foil viewed parallel to the feldspar **a** axis (with no perspective) illustrating the location and approximate thicknesses of amorphous sidewalls relative to the undamaged core of the foil.

3 μm wide and 1 μm thick was laid down by the same process. The initial stages of milling were performed automatically by the FIB computer, which followed a program optimized for silicon substrates. After initial milling at 5000–1000 pA, a foil 15 μm long by ~6 μm deep and 1.0 μm thick remained. The sides and bottom of the foil were then cut from the host grain, leaving it supported solely by the Pt strap. In the final "polishing" stage, the foil was thinned to ~800 nm by manually positioning the ion beam, then two thin windows were cut, one to ~200 nm and another to ~110 nm in thickness; during this phase, ion currents of 100–10 pA were used and the ion beam was oriented at an angle of ~1.2° to the plane of the foil. After removal of the supporting Pt by ion milling, the ~110 nm thick foil was lifted from the grain using an ex-situ micromanipulator and placed on a holey carbon film for study.

The foils were imaged initially using a STEM detector on the Quanta 200 SEM operated at 20 kV [hereafter these are termed low-voltage (LV) STEM images to distinguish them from STEM images formed using conventional high-voltage STEM microscopes]. As the foils are of approximately uniform thickness, most contrast in the dark-field LV-STEM images is from spatial variations in atomic mass (Lee and Smith 2006), and the LV-STEM was especially good for imaging the overall structure of the sample and for determining the thickness of the Au and Pt layers (Smith et al. 2006). Owing to the low accelerating voltages used, LV-STEM is also especially useful for imaging the ultrastructure of unstained or labeled biological materials (Takaoka and Hasegawa 2006). TEM work used two FEI Tecnai microscopes both operated at 200 kV, a T20 LaB_6 instrument for acquisition of selected area electron diffraction (SAED) patterns and diffraction contrast images, and a TF20 field-emission microscope for lattice imaging and energy-dispersive X-ray microanalysis. SAED patterns were acquired using photographic film, but all images were digitally captured. Of interest in this study is the potential presence and thickness of amorphous layers immediately beneath outer grain surfaces. In this context, it is important to note that the observed thickness of such a layer in a TEM image will depend on the orientation of the foil relative to the electron beam and the thickness of its undamaged core, which will be somewhat less than the ~100 nm thickness of the entire foil (Fig. 1). We estimate that with the foil oriented such that the electron beam was nearly parallel to [020] (an orientation whereby the feldspar would be diffracting strongly, thus giving maximum contrast with any amorphous layers, which necessitated ~2–4° of tilt), the observed thickness of any amorphous layer would have been ~2.5 nm less than its true value. Furthermore, the outermost ~2.5 nm of the feldspar sample, be it crystalline or amorphous, would probably not be observable.

Results

ESEM imaging of grain surfaces

Secondary electron ESEM images show that surfaces of grains still within the soil are remarkably clean (Figs. 2a and 2b) except for occasional microbial filaments, bacteria, and numerous micrometer-sized silica disks, which are interpreted to be the disarticulated remains of silica-scaled chrysophytes (also known as golden algae). Grain surfaces parallel to (001) and (010) are cut by ~0.3–0.5 μm wide by tens of micrometer long channels that have formed by the coalescence of lines of etch pits associated with semicoherent albite lamellae (Figs. 2a and 2b). Images of the sample when within the stability field of liquid water (i.e., ~1 °C/690 Pa) show that the channels are water filled (Fig. 2a), and these structures can extend throughout small grains forming lines of weakness parallel to $(\bar{6}01)$ along which the grains can disarticulate (Fig. 2b).

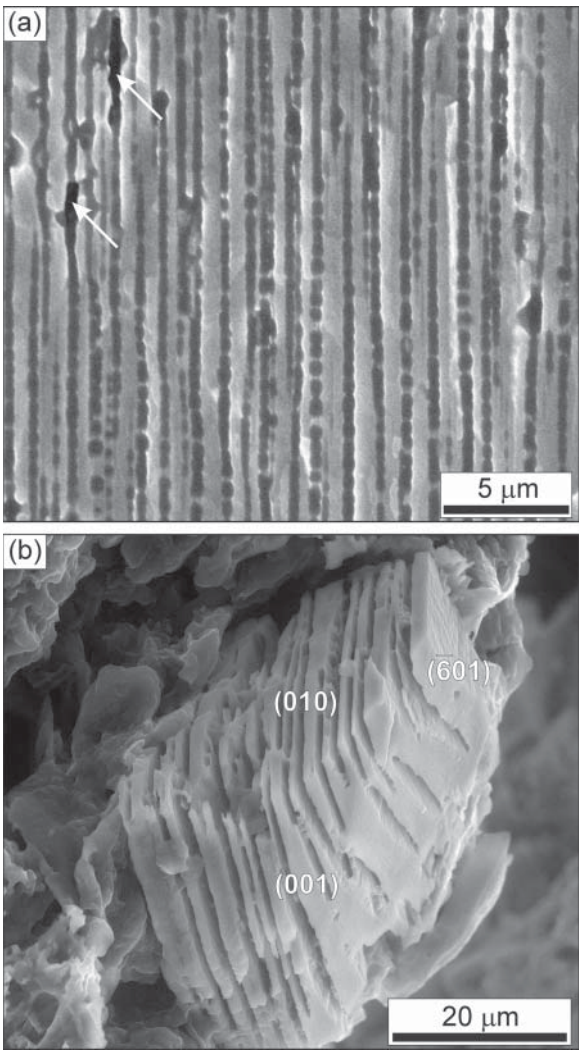

Figure 2. Secondary electron ESEM images of alkali feldspar grains contained within peat. (**a**) Etch channels on a heavily weathered (001) cleavage surface. Parts of two of the channels are empty and so are black in the image (arrowed), whereas most channels have a different (mid-gray) contrast because they are filled by liquid water (image acquired at +1 °C/690 Pa). (**b**) A grain dissected by etch channels. The approximate crystallographic orientations of grain surfaces are indicated (image acquired at +1 °C/630 Pa).

Crystallinity of grain surfaces in cross-section

Foils were cut initially from the surfaces of weathered grains with a relatively thin coat of Au, which was deposited as ~20–30 nm thick "islands" between which the base of the Pt strap is in direct contact with the grain surface (Fig. 3a). The outermost ~55–65 nm of these grains is amorphous (Fig. 3a), and the interface between the amorphous material and crystalline feldspar shows micrometer-scale relief but is sharp on the sub-nanometer scale (Fig. 3b). Qualitative X-ray microanalysis shows that the amorphous regions are compositionally similar to underlying feldspar but enriched in Ga. Those weathered grains with thicker (>~100 nm) and continuous Au coats are crystalline throughout so that an approximate inverse correlation can be recognized between thickness of the Au and underlying amorphous layer. The same relationship between thickness of the Au coat and amorphous layer was found in unweathered Shap feldspars, confirming that the tens of nanometers thick amorphous layers are artifacts of sample preparation and that a thick Au coat can preserve the integrity of near-surface regions of feldspars during ion milling.

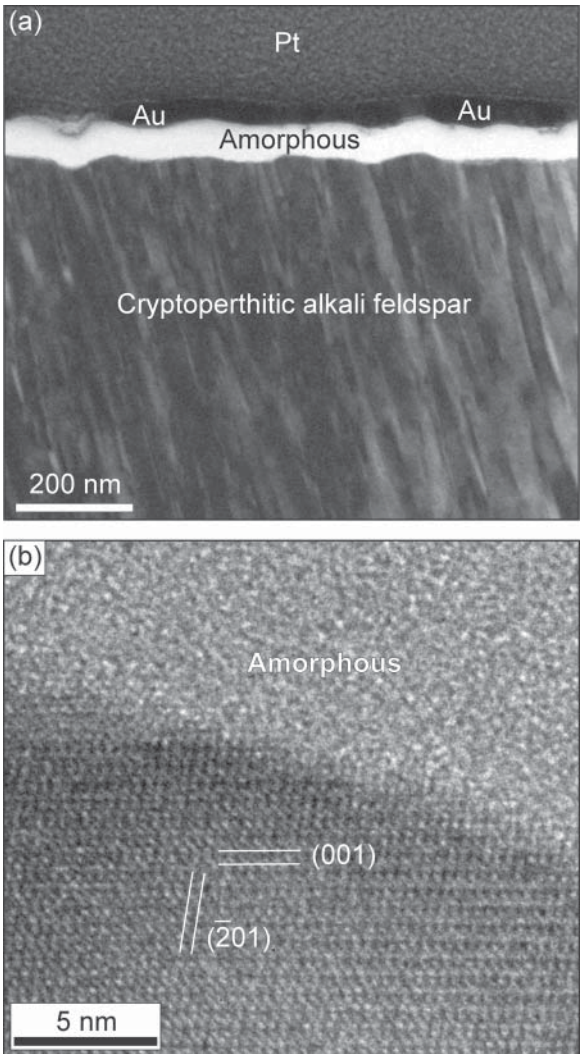

FIGURE 3. TEM images of a foil cut from a naturally weathered (001) alkali feldspar grain surface with the electron beam near [020]. (**a**) Bright-field diffraction contrast image of a cryptoperthitic alkali feldspar that was coated with ~35 nm of Au prior to FIB work. A ~60 nm amorphous layer is present beneath the Au and is thickest on the left hand side of the image where the Au is locally absent. (**b**) Lattice image of the interface between crystalline feldspar and amorphous material. It is highly likely that additional amorphization took place during TEM imaging.

There was no evidence for damage to the surface or near-surface regions of the unweathered control samples with a thick Au coat, but the sputtered Au atoms, ions, and particles could potentially damage delicate structures on weathered grain surfaces. To evaluate this possibility, several foils were manufactured from areas where the chrysophyte silica-scales rest on the grain surface (Fig. 4a). The silica-scales are unlikely to modify the underlying feldspar but are sufficiently thick to protect the grain surface from any damage during Au coating and ion milling. TEM images show that the grain is crystalline throughout where the silica-scale is in direct contact with its outer surface (Figs. 4b), but a ~20–50 nm amorphous layer is present where the tip of the silica-scale projects over a 60 nm step and has prevented deposition of Au and Pt on the grain surface beneath (Fig. 4c). This amorphous layer thins abruptly where the Au coat thickens beyond the tip of the silica-scale but the grain surface remains at the same level. On the left hand side of Figure 4c, the grain surface has a thick coating of Au and is crystalline throughout except for an extremely thin (~3 nm) non- or weakly diffracting layer. Further characterization of this layer was hindered by rapid rates of amorphization accompanying the intense electron irradiation required for high-resolution imaging and X-ray microanalysis. Such electron beam damage results in a dramatic reduction in the heights of the Na$K\alpha$ and K$K\alpha$ peaks relative to O$K\alpha$ and Si$K\alpha$ and a smaller reduction in the relative height of the Al$K\alpha$ peak.

Microtopography of grain surfaces and etch pit development

The surfaces of all weathered grains have steps (Fig. 4a), some of which correspond to the sites where underlying microtextures meet the grain surface. The 60 nm step in Figure 4b occurs at the outcrop of the L2 exsolution lamella whereas the ~0.8 μm step (Fig. 4d) is coincident with the point where an orthoclase subgrain intersects the weathered surface. A small etch pit has formed along one of the subgrain boundaries (Fig. 4d), but most of the pits occur at the outcrops of albite lamellae, producing lines of pits aligned parallel to **b** and the trace of ($\bar{6}$01) (Figs. 4a and 5a). The size, shape, and interconnectivity of these pits is determined by the width and coherency of albite lamellae and degree of weathering. The lamellae in Figures 4a and 4b are relatively narrow (L1 and L2 are 160 and 60 nm wide, respectively) and associated etch pits are correspondingly small and shallow at this stage of weathering. The contrasting weathering styles of coherent and semicoherent lamellae is especially clear in Figure 5a where a ~90 nm wide semicoherent lamella with associated equant etch pits is enclosed within a volume of coherent cryptoperthite, and very fine-scale corrugations have formed where this microtexture meets the grain surface. TEM images of a foil cut from a nearby area of this sample show that in cross-section these corrugations comprise shallow asymmetric troughs separated by sharp crests (Fig. 5b). Albite platelets 20–40 nm in

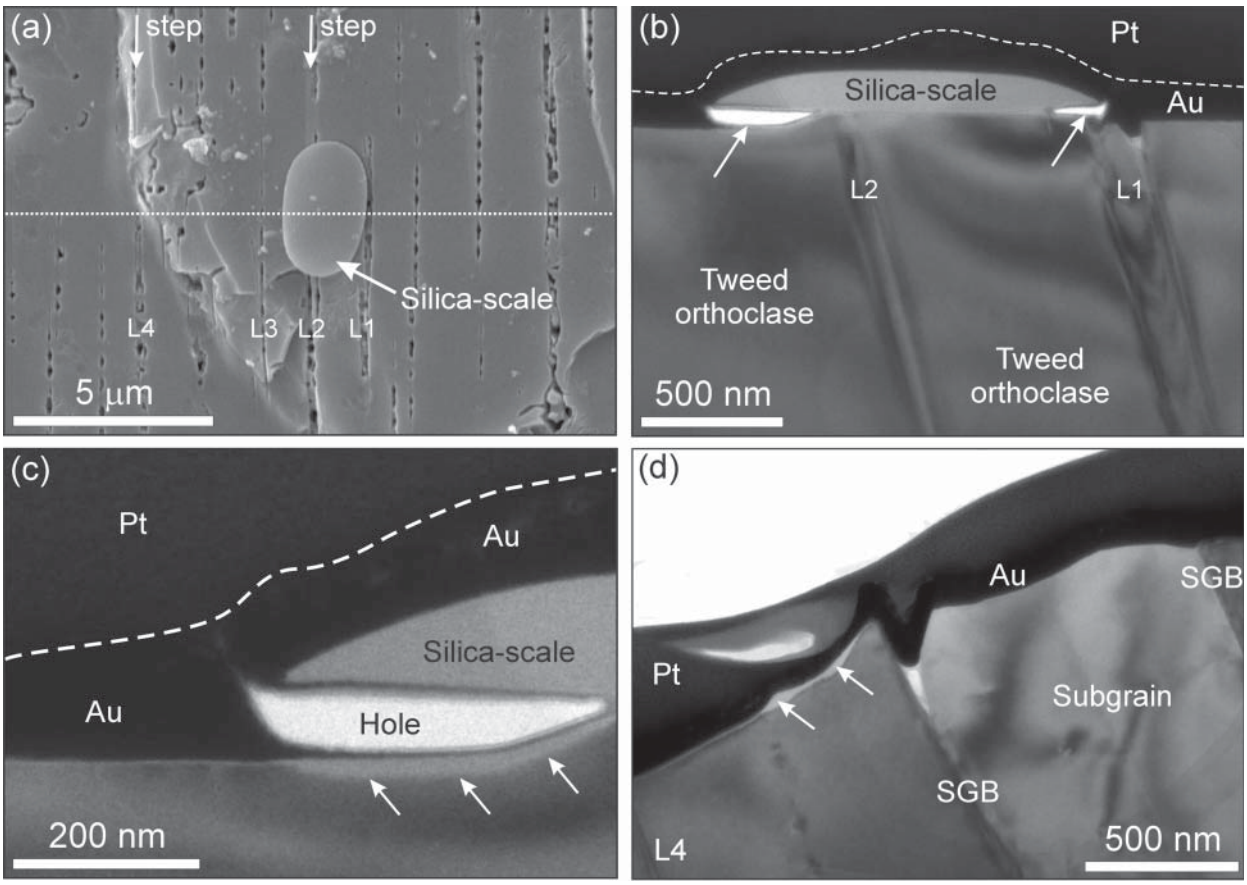

Figure 4. Images of a naturally weathered alkali feldspar grain. (**a**) Secondary electron SEM image of a silica-scale resting on a (001) grain surface. L1–L4 identify the pitted outcrops of individual albite exsolution lamellae. There are several steps on the grain surface, and the two that were studied in cross-section are indicated by arrows; one is ~800 nm high (left of center) and the other ~60 nm high and coincident with the outcrop of L2. Although here called steps both have relatively low angle slopes. The midplane of the foil is indicated by a dotted white line. (**b**–**d**) are bright-field diffraction contrast TEM images, with the electron beam near [020]. (**b**) Image of an area that includes the silica-scale, L1, L2, and the step next to L2. Areas beneath the leading edges of the silica-scale (now holes in the foil, indicated by arrows) were shielded from Au and Pt deposition. (**c**) Image of the left hand side of **b**. A ≤20 nm thick amorphous layer (arrowed) is present where the leading edge of the silica-scale projects over the step. (**d**) Image of the part of the foil that includes the ~800 nm step. The upper part of the step has formed where an orthoclase subgrain intersects the surface. A narrow and shallow etch pit, now largely Au filled, has developed by dissolution of the subgrain boundary (SGB) at the image center. An amorphous layer an average of 25 nm thick is present at the grain surface (arrowed) where the overlying Au coat is ~50 nm thick.

width intersect the grain surface at the floors of the troughs, and all areas between are composed of orthoclase (Fig. 5b), indicating that dissolution is concentrated on the albite platelets. There is also a good positive correlation between the separation of troughs (i.e., the spacing of albite platelets, which ranges from ~50–165 nm) and the height of the intervening crest (~7–35 nm above the floors of surrounding troughs, Fig. 5c).

The deeper etch pits on weathered (001) surfaces have formed by dissolution concentrated on the outcrops of dislocation loops that encircle semicoherent albite lamellae in the **a-c** plane (Figs. 5a and 6a), but those loops oriented parallel to **b** may also be etched as the two sets of dislocations are connected in the Murchison plane. TEM images of a foil from the grain in Figure 6a show that the semicoherent lamellae are cut by ~30–50 nm wide holes that extend into enclosing orthoclase (Fig. 6b). The regular morphology of these holes demonstrates that they are not ion-milling artifacts but "etch tubes," which were identified initially in the Shap feldspars by Lee and Parsons (1995). These structures have formed long after the nanotunnels described by Fitz Gerald et al. (2006), although both the etch tubes and nanotunnels have resulted from dissolution centered on elastically strained feldspar surrounding the cores of misfit dislocations. In bright-field TEM images the etch tubes have an amorphous rim a few tens of nanometers in thickness (Fig. 6b). The outer edge of the rim is dark and uniform in thickness, whereas the inner part, adjacent to the feldspar, is lighter and ~1.5 times thicker on the lower than upper side of the tube (relative to the orientation of the grain during ion milling). As discussed below, rims around holes in this sample and others are interpreted to be ion-milling artifacts. With progressive weathering, etch pits on (001) grain surfaces coalesce to form wider and more continuous parallel-sided channels that extend for many micrometers beneath the

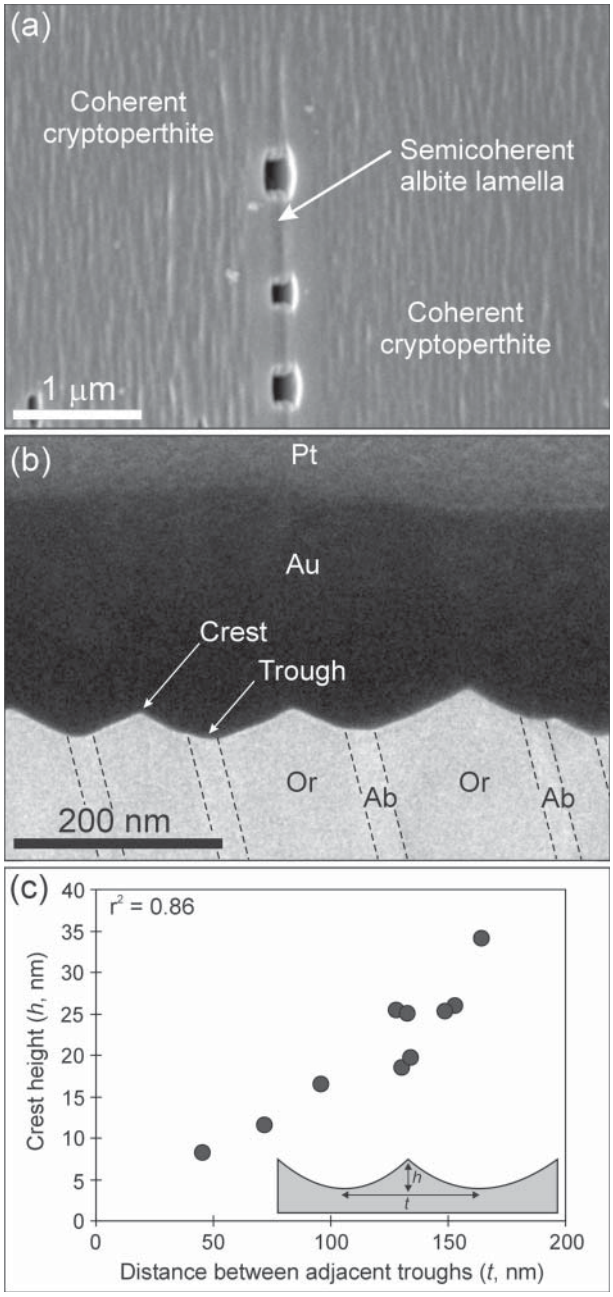

FIGURE 5. (**a**) Secondary electron SEM image of fine-scale corrugations on a naturally weathered (001) grain surface that have formed where coherent albite platelets intersect the surface. Three larger equant pits occur along the outcrop of a semicoherent albite lamella. (**b**) Bright-field TEM image of a foil cut from a corrugated (001) surface in a slightly different part of the grain compared to **a** with the electron beam near [020]. Albite platelets (Ab) meet the grain surface at the floors of troughs. Owing to low contrast with tweed orthoclase (Or) within which the crests have developed, the edges of the albite platelets are delineated by dashed black lines. The thick Au coat and overlying Pt strap are indicated. (**c**) Plot of crest height against the spacing of intervening troughs using measurements from TEM images including that shown in **b**.

grain surface, beyond which are etched remnants of albite (Fig. 6c). Feldspar that survives between the etch pits is predominantly tweed orthoclase, but can contain coherent albite platelets, and shallow asymmetrical troughs are again developed where the platelets meet the weathered grain surface (Fig. 6d).

Microbial filaments are occasionally found on grain surfaces and, although their biological affinity is difficult to determine with certainty, their size and shape is similar to that of fungal hyphae. A foil was cut from an area where a filament had a patchy coating (Fig. 7a), which was believed initially to be an accumulation of weathering products. The filament was imaged by LV-STEM to check for any internal structure (the low kV electron beam should be scattered very effectively by the organic material), but little was found using bright- or dark-field imaging (Fig. 7b). There is also negligible contrast between the filament and the coating, although some variations in mass and internal structure within the coating are apparent in the vicinity of L6 (Fig. 7c). Diffraction-contrast TEM shows that both the filament and coating are amorphous (Fig. 7c), and, so together, these observations are consistent with the coating being predominantly organic in origin and not a silicate weathering product. X-ray spectra demonstrate that the filament and coating are enriched in Ca and O relative to the feldspar, and some spectra also show trace concentrations of Fe. Phosphorous is another element that may be useful in assessing the degree of chemical preservation of the filament, but was difficult to identify owing to an overlap between the P*K*α peak (2.01 keV) and those of Pt*M*α (2.05 keV) and Au*M*α (2.12 keV).

As the grain surface in this foil is overlain by the amorphous organic material, an amorphous Si-rich layer, which may have potentially formed by weathering of the feldspar, would be very difficult to detect in the TEM images. However, the presence of the micropores within the coating constrain any amorphous layer between the feldspar and micropores to being <7 nm in thickness. These images also illustrate clearly the difference in weathering styles between coherent albite platelets, which dissolve to produce shallow corrugations at the grain surface, and semicoherent albite lamellae within which coarser etch pits and etch tubes develop. The degree of weathering in this grain ranges from pairs of shallow pits and narrow tubes straddling the lamellae (e.g., L6 in Fig. 7c) to continuous tubes that can extend >7 μm into the grain interior (e.g., L3 in Fig. 7b). The etch tubes again have amorphous rims, and dark-field LV-STEM images show that the darker outer rims scatter electrons much more effectively than the inner lighter rims or surrounding feldspar (Fig. 7b). This contrast indicates that the outer rims have a considerably greater atomic mass than the feldspar, which is consistent with enrichment of the amorphous material in Ga^+ by implantation and/or redeposition.

DISCUSSION

Artifacts from Ga^+ ion implantation

The ≤~65 nm thick amorphous layers beneath the surfaces of naturally weathered and unweathered alkali feldspars with discontinuous and/or thin Au coats are interpreted to form in the FIB as a result of implantation of 30 kV Ga^+ ions during initial imaging and deposition of the Pt grounding layer and

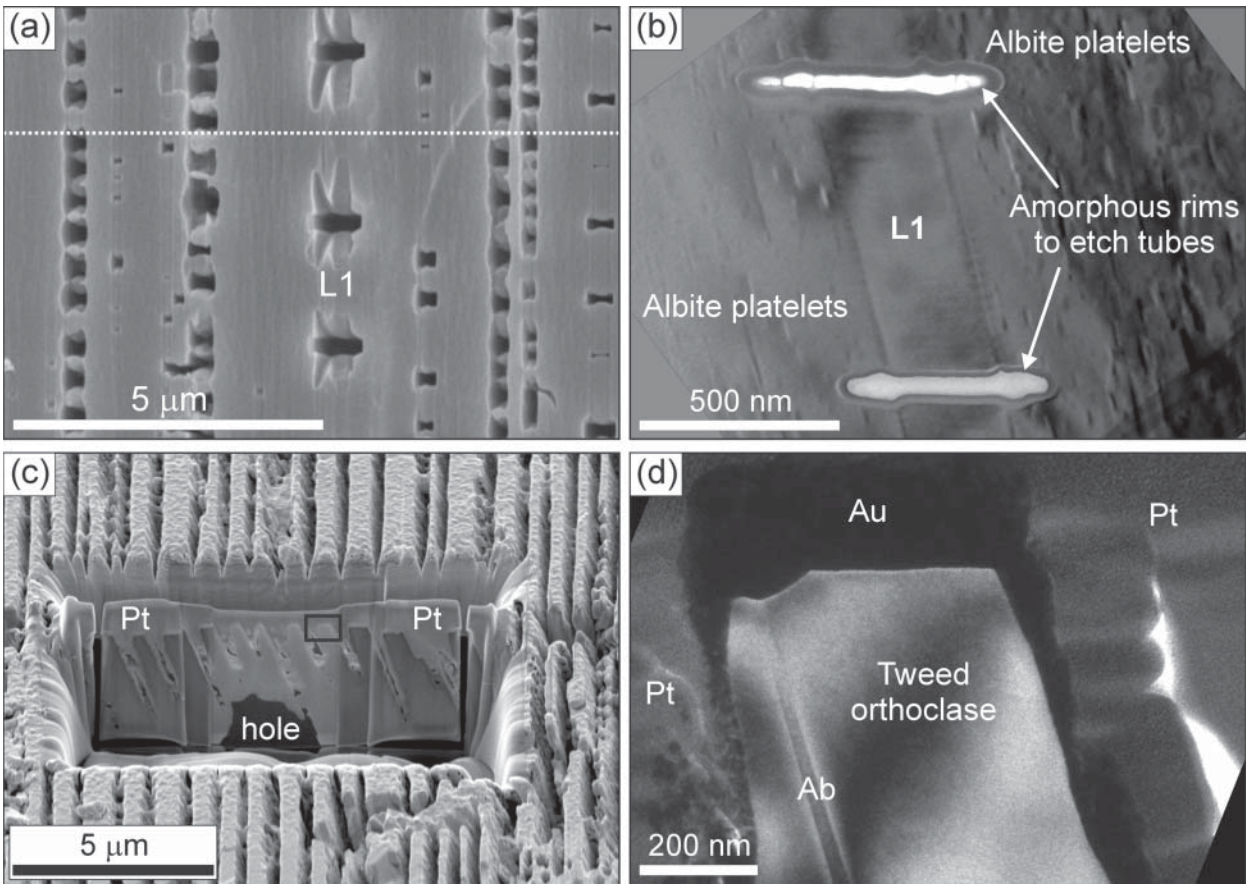

Figure 6. Images of naturally weathered alkali feldspars: (**a**) and (**c**) are secondary electron SEM images of (001) grain surfaces, and (**b**) and (**d**) are bright-field diffraction contrast TEM images of foils cut from **a** and **c**, respectively and oriented with the electron beam near [020]. (**a**) Lines of etch pits have formed where semicoherent albite lamellae intersect the grain surface; one prominent lamella is labeled L1. Shallow corrugations between the lamellae have formed at the outcrops of coherent albite platelets. The midplane of the foil is indicated by a dotted white line. (**b**) Image of part of a foil cut from the grain surface in (**a**). The image shows the region of lamella L1 that is 4.0–5.5 μm below the outer grain surface. The lamella is Pericline twinned and is cut by two etch tubes that extend into surrounding orthoclase. Each tube has an amorphous rim whose inner part (i.e., abutting the feldspar) is lighter than the outer part and the middle of the tube is empty (white in this image). (**c**) A heavily weathered (001) surface where semicoherent albite lamellae have been dissolved to form long and narrow etch channels. The sample has been tilted at 48° away from the reader so that the foil prior to lift-out can be seen. Part of the base of the foil was lost during milling to leave a hole. The Pt strap is also indicated. (**d**) Image of the boxed area in **c**. Feldspar remaining between the channels consists of tweed orthoclase containing a narrow coherent albite lamella (Ab) and a small etch pit occurs where albite meets the outer grain surface. Note the strain contrast along both sides of the lamella. The feldspar is coated with Au, which thins along the sub-vertical etch pit walls, and the surrounding etch pits are near-completely filled by Pt. The tweed orthoclase is crystalline throughout.

strap. Although the role of the Pt is to protect the substrate, Ga^+ ions used for Pt deposition will be able to reach the grain surface until a thickness of Pt sufficient to stop them has accumulated. The profile of implantation of 30 kV Ga^+ ions into feldspar was modeled using the stopping and range of ions in matter (SRIM, version 2003.26, Ziegler 2003) with a soda-lime glass substrate (density 2.56 g/cm^3) as a proxy. Results show that the maximum depth of Ga^+ implantation is ~50 nm, although the Ga concentration peaks at ~25–30 nm below the grain surface. However, production of vacancies by collision of Ga^+ ions with feldspar is a better expression of damage, and the SRIM model shows that the peak occurs at ~15–20 nm beneath the surface with almost no vacancies being created below ~50 nm. This value is somewhat less than our observed depth of amorphization of 65 nm and one possible explanation for this discrepancy is that the glass is a poor proxy for feldspar. Amorphous layers have also been found in previous studies beneath the top surfaces of synthetic crystalline materials that were uncoated prior to FIB work or had thin Au or Pt-Pd coatings, although these layers are thinner (≤48 nm) than recorded in the present study (Table 1), indicating that feldspar may be especially susceptible to amorphization by ion irradiation. As the amorphized material has a composition similar to the precursor feldspar, apart from elevated Ga concentrations, damage to the feldspar crystal structure by ion irradiation must differ fundamentally from that induced by electron irradiation, which leads to a dramatic loss of Na and K. Note that previous work on

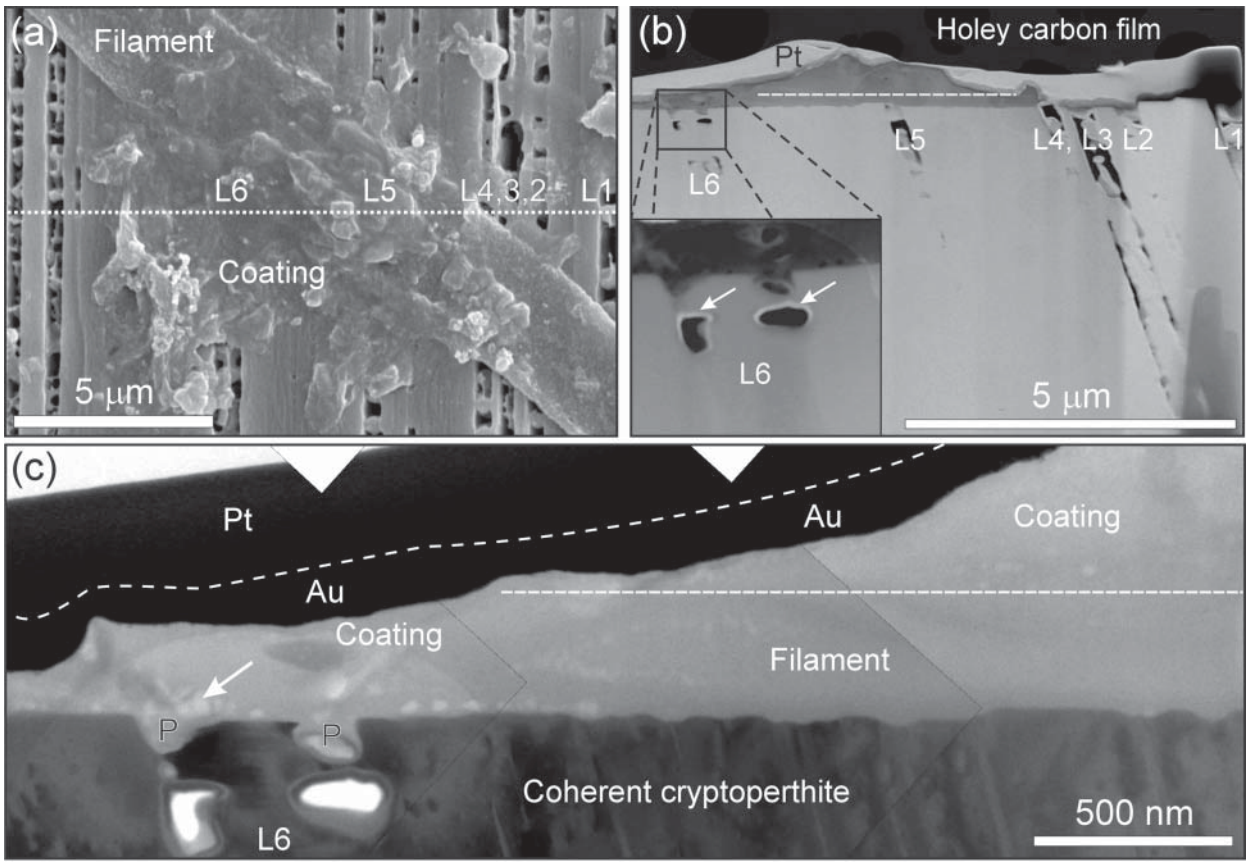

FIGURE 7. Images of a weathered (001) grain surface overlain by a microbial filament and coating. (**a**) Secondary electron SEM image showing the filament and etch channels that have formed where semicoherent albite lamellae, numbered L1 to L6, intersect the grain surface. Part of the filament and adjacent grain surface has a structureless coating. The midplane of the foil is indicated by a dotted white line. (**b**) Dark-field LV-STEM image of the foil. The etched lamellae are again labeled (L1–L6) and some of the etch pits seen on the grain surface extend as ~50–300 nm wide tubes at least to the base of the foil 5 μm beneath the grain surface. The microbial filament and coating both have a lower atomic mass and so darker in this image than the feldspar and a dashed white line indicates the approximate interface of the filament (below) and coating (above). Platinum denotes the platinum strap that overlies an Au coat. The inset dark-field LV-STEM image shows two etch tubes within L6 (arrowed) whose rims are bright owing to their relatively high atomic mass. (**c**) Montage of three bright-field diffraction-contrast TEM images of the grain surface in the vicinity of L6 (electron beam near [020]). A dashed white line delineates the approximate contact of the filament with overlying coating. The left hand edge of the filament is approximately at the point where L6 intersects the grain surface. The feldspar to the right of L6 is a cryptoperthite and shallow corrugations have formed where coherent albite platelets intersect but grain surface. A pair of larger pits (labeled P) straddle the outcrop of L6. In the vicinity of L6 the coating contains micropores (arrowed) that constrain any amorphous layer at the feldspar grain surface to being <~7 nm thick.

FIB-induced damage to semiconductor and silicon substrates has concluded that the thickness of the amorphized layer is strongly dependent on ion-beam energy, but independent of current (Kato 2004; Rubanov and Munroe 2004). As the accelerating voltage (30 kV) and current (300 pA) used for deposition of Pt was not varied between experiments undertaken here, we cannot test the conclusions of these studies.

The sidewalls of the foil also undergo damage during low angle (~1°) ion polishing prior to lifting out. We did not experimentally determine the thickness of sidewall amorphous layers, but SRIM modeling showed that the maximum depth of vacancy formation in soda-lime glass under our experimental conditions (i.e., 30 kV) is ~20 nm (Table 1). If a linear relationship between the thickness of the top surface and sidewall damage layers in any one material is assumed [i.e., the Si/Si p-n junction described by Wang et al. (2005) would be 48/20 nm or 2.4/1, Table 1], the sidewall damage layer for alkali feldspars should be ~27 nm (i.e., 65 nm/2.4), which is greater than the modeled value (~20 nm) and the thickness of sidewall amorphous layers experimentally determined from synthetic materials (Table 1). If both sidewalls have this depth of damage, ~50% of each ~100 nm thick feldspar foil would be amorphous, but diffraction contrast and lattice images could nevertheless be acquired from its ~50 nm thick undamaged core. These results do, however, suggest that the integrity of a feldspar foil would be lost if milled to thickness significantly less than 100 nm using 30 kV Ga^+ ions. Any change in chemical composition accompanying amorphization of the sidewalls will also have important implications for interpretation of results from TEM energy dispersive X-ray microanalysis or electron energy loss spectroscopy, although apart for enrichment in Ga, the composition of alkali feldspar appears to change little as a consequence of ion-beam damage.

TABLE 1. Thicknesses of amorphous layers on the top surfaces and sidewalls of foils cut from different substrates using 30 kV Ga^+ ions

Substrate	Top surface (ion beam at 90°)		Sidewall (ion beam at ~1°)
	Coating	Amorphous layer thickness	Amorphous layer thickness
AlAs-InAs superlattice*	<15 nm of Au	~25 nm	nd
AlAs-InAs superlattice*	>60 nm of Au	0 nm	nd
Alkali feldspar†	~25 nm Au "islands"	~65 nm	nd
Alkali feldspar†	>100 nm of Au	0 nm	nd
Si/Si p-n junction‡	none	48 nm	20 nm
Si/Si p-n junction‡	>50 nm Pt-Pd	0 nm	nd
Silicon§	na	na	21 nm
Soda lime glass‖	none	50 nm	20 nm
$CaCO_3$#	na	na	40 nm
CH_2O#	na	na	64 nm

Note: na denotes not applicable and nd denotes not determined.
* Experimentally determined by Rubanov and Munroe (2003).
† The present study.
‡ Experimentally determined by Wang et al. (2005).
§ Experimentally determined by Kato (2004).
‖ Maximum depth of vacancy formation modeled by SRIM for this study using a glass density of 2.56 g/cm^3.
Modeled using SRIM by Obst et al. (2005).

Sidewall amorphization can be minimized by using less energetic Ga^+ ions during final polishing, but also reducing the beam current may have little impact because Kato (2004) has found no relationship between thicknesses of sidewall amorphous layers and beam current or the duration of milling. Amorphization was also found around holes that were present within samples prior to ion milling, such as those beneath silica-scales (Fig. 4c) and the etch tubes within grain interiors (Figs. 6b, 7b, and 7c). The amorphous layer on the feldspar beneath the projecting tip of the chrysophyte silica-scale in Figure 4c has clearly formed by ion implantation, possibly with some additional redeposition of sputtered material, as it occurs only where the Au and Pt are absent. The amorphous rims around tubes in grain interiors are more complex in structure. As those parts of the rims that are lighter in bright-field TEM images are thicker on the lower than upper side of the tube, they are also inferred to have formed by Ga^+ implantation during low-angle polishing. The outer parts of the rims, which are of a uniform thickness and a greater atomic mass than the feldspar, are inferred to have formed by redeposition during milling, which typically results in much greater levels of Ga-enrichment than ion implantation (Rubanov and Munroe 2004; Liu and Jiao 2005).

Owing to the low accelerating voltages used in LV-STEM imaging, it is an especially useful technique for imaging the ultrastructure of unstained biological samples (Takaoka and Hasegawa 2006), but little internal structure could be identified within the microbial filament (Fig. 7b). This could be because the filament had partly decayed prior to sampling or because it had undergone damage during Ga^+ ion milling. These two possibilities are difficult to distinguish with the information available, but the same poor preservation of internal structure was found in FIB and TEM studies by Obst et al. (2005), who cross-sectioned a cyanobacterium, and Benzerara et al. (2005a, 2005b) in their study of a microbial filament similar to that in Figure 7. Results of SRIM modeling by Obst et al. (2005) indicated that the ~64 nm thick amorphous sidewalls within the cyanobacterium were responsible for loss of biological structure. Despite this poor structural preservation, both of the aforementioned studies found that a proportion of the original chemical constituents had been retained, including polysaccharides and proteins (Benzerara et al. 2005a).

Mitigation of ion damage to outer grain surfaces

Ion-beam damage to outer grain surfaces can be prevented by coating them with a layer of Au or Pt-Pd of sufficient thickness to stop high-energy Ga^+ ions. Previous work on synthetic materials has shown that a minimum thicknesses of 50–60 nm (Table 1) is required to prevent amorphization of near-surface regions of the substrate by 30 kV Ga^+ ions. By contrast, >100 nm of Au was required to ensure that Shap feldspar grain surfaces remained undamaged during ion imaging and Pt deposition, although current work on grains from other localities indicates that amorphization can be prevented by ~80–85 nm of Au. This value is still greater than the thickness of Au or Pt-Pd required to protect synthetic materials, and one potential explanation for this discrepancy is a contrast in the composition or porosity of coatings applied in different studies. A more likely reason is that as the coating thickness required to protect a surface is assessed from the degree of amorphization of the substrate, a material that is more resistant to implantation of Ga^+ ions, such as a Si/Si p-n junction (Table 1), will require a thinner coat than one that is more susceptible to damage such as alkali feldspar. SRIM modeling indicates that 30 kV Ga^+ ions will penetrate a maximum of 25 nm into Au whereas observations in this study show that the ions can penetrate <~80 nm of Au to amorphize the underlying feldspar. This apparent discrepancy between calculated and observed stopping distances is probably due to differences in density between the pure Au substrate assumed in the modeling and porous Au layers deposited by sputtering. If initial imaging and deposition of the Pt strap is undertaken using an electron beam in a dual-beam FIB, some of the problems described above can be overcome, although a thin Au coat will still be required to mitigate charging of insulating samples.

Gold coatings are clearly important for protecting grain surfaces, but the atoms, ions, and nanometer-sized particles sputtered from the Au target could also damage the surface to form a thin amorphous layer (Behrisch 1981). For most FIB applications, the possibility of such damage is of little consequence, but in this study, the presence of a thin amorphous layer could be indicative of non-stoichiometric dissolution of the Shap feldspars, or precipitation of non-crystalline reaction products during weathering, and so damage by sputtered Au may be important. Foils cut from some weathered grain surfaces showed a very thin (~3 nm) non-diffracting or weakly diffracting layer between the feldspar and the Au, but further characterization was hindered by electron beam damage rendering the feldspar amorphous, and the layers may in fact owe their origin to a slight distortion of feldspar crystal structure by strain at the grain surface. Although we were unable to calculate the damage caused by Au particles, SRIM modeling shows that 1 kV Au ions with an angle of incidence of 90° will be implanted to a depth of ~5 nm into a soda-lime glass substrate. However, the impact energies of Au particles are likely to be far less than the kV used during sputtering (R. Chater, personal communication) and if so, the

value of 5 nm will be considerably greater than the true depth of implantation and damage. Although little previous work has been done on damage by sputter coating, a FIB, and TEM study by Rubanov and Munroe (2003) showed that the outermost 2 nm thick layer of an AlAs-InAs superlattice substrate was preserved intact beneath the sputtered Au coat, indicating very little damage to this material coated under one set of conditions. We conclude that Au coating causes no identifiable damage to weathered feldspar surfaces. If the sample can be imaged and Pt deposited using an electron beam in a dual-beam FIB a carbon coat may be sufficient to neutralize charging of insulating samples, although such a coating may provide insufficient protection from impacting Pt ions and particles.

Impact of natural weathering on feldspar crystallinity

As described above, the presence of an amorphous "leached" layer or non-crystalline precipitate immediately beneath grain surfaces would provide important information on the mechanisms of chemical weathering within the Shap soils. As far as the authors know, amorphous layers have not been previously described by TEM from feldspars recovered from soils, and Benzerara et al. (2005a, 2005b) found that the weathered surface of an OPX grain from a Saharan meteorite was crystalline throughout except where encrusted by a microbial filament (discussed below). Amorphous layers ~10 nm in thickness have been described on detrital alkali feldspar grains from a sandstone aquifer by Zhu et al. (2004). In this case the amorphous layer, which was depleted in K relative to the feldspar, was overlain by kaolinite and smectite, although it is unclear from their description whether this is a residual layer produced by leaching of ions from the feldspar substrate or an amorphous reaction product. Kawano and Tomita (2001) have also described 50–100 nm thick amorphous layers on the surfaces of An-rich plagioclase crystals erupted from a Japanese volcano. It is important to emphasize that mechanisms and rates of weathering differ significantly between feldspars within the plagioclase series and between plagioclase and alkali feldspars so that comparisons between studies must be made with care.

Results of this study have provided no evidence for amorphous layers >~2.5 nm in thickness beneath the Au coated outer surfaces of grains or sub-vertical walls of etch pits. It is possible that near-surface regions of the Shap feldspars could have been rendered non-stoichiometric by selective removal of some ions, such as Na^+ and K^+, whilst maintaining the integrity of the framework but this could not be tested by TEM owing to the susceptibility of alkali feldspar to amorphization and loss of alkali ions during chemical analysis using nm-sized electron probes. A thin (<7 nm) amorphous layer may be present beneath the microbial filament encrusting the Shap feldspar and Benzerara et al. (2005b) did find poorly crystalline aluminosilicate weathering products beneath the filament on a meteoritic OPX grain. However, Barker and Banfield (1996) were unable to find any evidence for "leached layers" on the outer surfaces of ultramicrotomed mineral grains including feldspars that had been weathered by lichens. As results of the present study are clearly at odds with the common finding of amorphous layers on feldspars and other silicate minerals used in laboratory dissolution experiments (e.g., Hellmann et al. 2003), and descriptions of non-stoichiometric (but not necessarily amorphous) layers immediately beneath the surfaces of plagioclase feldspars recovered from soils (e.g., Nugent et al. 1998), much more work needs to be done to characterize both the composition and crystal structure of naturally weathered mineral surfaces. By undertaking X-ray photoelectron spectroscopy (XPS) work on the Shap feldspars, their near-surface chemistry can be compared directly with their structure as revealed by TEM, and preliminary XPS results do indicate that the outermost few nanometers of the Shap grains may differ in chemical composition from the bulk. These results will be presented and discussed further in a subsequent publication.

Microtopography and the internal zone

TEM images of foils demonstrate that some of the steps on grain surfaces are coincident with the outcrops of exsolution lamellae and subgrains, and are interpreted to form where intracrystalline microtextures influence the trajectory of fractures propagating through the grains during physical weathering. This process can be recreated during laboratory crushing of perthitic alkali feldspars and makes a major contribution to their surface roughness (Hodson et al. 1997). Xu (1997) and Xu et al. (2000) showed that the feldspar crystal structure can influence the way in which grains break on a much finer scale. Using scanning probe microscopy (SPM), they found 0.66 and 0.30 nm sized steps on (001) cleavage surfaces of a cryptomesoperthite, which reflect the unit-cell dimensions of the feldspar, and ~0.5 nm scale corrugations where Albite twins within Ab-rich lamellae intersect the surface. Structures on such scales would be difficult to identify by TEM imaging of the FIB-produced foils.

The corrugated microtopography developed where cryptoperthites intersect the weathered surfaces of Shap feldspars is due to the greater dissolution rate of albite than orthoclase. Contrasts in the dissolution rates of the two minerals may be due purely to the differences in their chemical compositions, although compilations of data from laboratory experiments on feldspars indicates that the dissolution rates of albite and K-feldspar in acidic solutions are similar (Blum 1994). The other possibility is that differences in the magnitude of stored elastic strain energy could drive the contrasts in dissolution rates if the strain were distributed heterogeneously within the cryptoperthites. To retain coherency, albite must be in tension and orthoclase in compression in the plane of the interface; for example, the (001) planes of unstrained albite (d_{001} ~0.640 nm) must be expanded and orthoclase (d_{001} ~0.648 nm) compressed. X-ray diffraction work confirms that the unit-cell parameters of the Ab- and Or-rich feldspar components of coherent cryptoperthites deviate considerably from the unstressed values (Smith and Brown 1988), and the total strain energy is ~2–3 kJ/mol in albite and orthoclase and 0.6–0.9 kJ/mol at the interface (Brown and Parsons 1993). The albite platelets should be more highly strained, per unit volume, than the dominant orthoclase, and the magnitude of strain within orthoclase should decrease with distance from albite platelets on either side, but would also be affected by the thicknesses of adjacent platelets and the presence of any others just outside of the plane of the foil. Thus, the correlation between spacing of troughs, centered on albite, and heights of intervening crests within orthoclase could be explained

in terms of dissolution picking out gradients in the magnitude of stored elastic strain, with volumes of orthoclase furthest from the albite platelets being least highly strained and having the lowest relative rates of dissolution.

Regardless of their driving force for dissolution, the chemical weathering rates of albite platelets are far slower than of adjacent semicoherent albite lamellae, which may largely reflect the ease with which solutions can gain access to the interiors of the coarser lamellae via etch pits at the grain surface and etch tubes in grain interiors. Previous work by Lee et al. (1998) had suggested that the etch pits and tubes in Shap feldspars formed by dissolution of the elastically highly strained feldspar surrounding the network of dislocations that enclose semicoherent albite lamellae and such strain-controlled weathering is commonplace in alkali feldspars (Eggleton and Buseck 1980; Banfield and Eggleton 1990). However, following the work of Fitz Gerald et al. (2006) on alkali feldspars from the Shap granite and other igneous and metamorphic rocks, it is now clear that the weathering solutions do not attack pristine strained crystal structure but instead exploit a network of nanopores provided by the nanotunnels and associated pull-aparts that form during cooling. Although the nanotunnels are generated by deuteric/hydrothermal dissolution of the elastically strained cores of misfit dislocations, the weathering solutions must widen the pores by attacking their walls, which will retain considerable elastic strain. Therefore, when these alkali feldspars enter the weathering regime they already possess a network of conduits, in effect an incipient "internal zone," which serves as a template, or guide, for subsequent weathering.

Previous TEM-based studies of feldspar weathering have described abundant intragranular clay mineral alteration products (e.g., Eggleton and Buseck 1980; Tazaki 1986; Banfield and Eggleton 1990; Sheets and Tettenhorst 1997). We found no evidence for accumulations of clay minerals >2.5 nm thick on the outer surfaces of Shap feldspars, but it may be expected that solutions within the intragranular nanopore networks would readily reach saturation with respect to weathering products and become clogged. The fact that semicoherent lamellae weather so effectively by growth and coalescence of etch pits and tubes suggests this does not happen and no clay minerals were found during this study. We conclude that dissolution rates of even the most highly strained feldspar are slower than rates of removal of ions from reaction sites by diffusion through the probably static pore fluids. On reaching the grain surface, these solutes must be effectively removed to and diluted within the bulk soil waters, which Lee et al. (1998) have shown are undersaturated with respect to potential precipitates. The differences in abundances of clay minerals found in the previous studies and the present work is therefore most probably due to contrasts in water to rock ratios of the weathering environments. It is also interesting to note that Benzerara et al. (2005a, 2005b) found an aluminosilicate beneath a microbial filament encrusting an OPX grain from a Saharan meteorite. The absence of clay beneath a morphologically similar filament on the Shap feldspar could simply be because insufficient time has been available, or due to much slower rates of organically mediated weathering of OPX and alkali feldspar. Although the Shap microbial filament encrusts a pitted grain surface, the presence of etch pits of comparable size elsewhere on the grain surface (Fig. 7a) indicates that the microorganism has had little direct impact on chemical weathering of the feldspar. Much more work on microbe-mineral interfaces needs to be undertaken to explain the contrasting conclusions from these two studies.

This work has shown that the combination of FIB and TEM techniques provides a unique insight into the natural weathering mechanisms of mineral grains, in particular how fluids may gain access to the grain interior and interact with the surface during dissolution and precipitation reactions. Results from such work must, however, be interpreted with particular caution owing to the ease with which the crystal structure of weathered (and unweathered) feldspar is destroyed and chemical compositions potentially modified by the high energy Ga^+ ions used in manufacture of the foils and intense electron irradiation accompanying high spatial resolution TEM imaging and chemical analysis. With the increasing availability of dual-beam FIB instruments, which can use an electron beam to locate areas of interest and deposit protective Pt, some of the artifacts highlighted in this study may be reduced, in particular amorphization of the top surface of the sample. However, we emphasize that dual-beam FIBs are not a panacea for all of the aforementioned difficulties and may create others that will need to be assessed by future work, for example, potential damage to the top surface of the sample during electron beam deposition of the Pt grounding layer and strap.

Acknowledgments

We thank Alan Craven for access to the FIB and TEM equipment in the Department of Physics and Astronomy, University of Glasgow, and Billy Smith and Colin How for their technical assistance. The manuscript has benefited considerably from helpful comments by Richard Chater (Imperial College) and very timely, careful and detailed reviews from Karim Benzerara, John Fitz Gerald, and Richard Wirth. This work was funded by the U.K. Natural Environment Research Council.

References cited

Anderson, R., Tracy, B., and Bravman, J., Eds. (1992) Specimen preparation for Transmission Electron Microscopy of materials. III. Materials Research Society, 254, Pittsburgh.

Banfield, J.F. and Eggleton, R.A. (1990) Analytical transmission electron microscope studies of plagioclase, muscovite and K-feldspar weathering. Clay and Clay Minerals, 38, 77–89.

Barker, W.W. and Banfield, J.F. (1996) Biologically versus inorganically mediated weathering reactions: Relationships between minerals and extracellular microbial polymers in lithobiontic communities. Chemical Geology, 132, 55–69.

Behrisch, R., Ed. (1981) Sputtering by particle bombardment I. Physical sputtering of single element solids. Topics in Applied Physics 47, Springer-Verlag, Berlin.

Benzerara, K., Yoon, T.H., Menguy, N., Tyliszczak, T., and Brown, G.E. (2005a) Nanoscale environments associated with bioweathering of a Mg-Fe-pyroxene. Proceedings of the National Academy of Sciences of the United States of America, 102, 979–982.

Benzerara, K., Menguy, N., Guyot, F., Vanni, C., and Gillet, P. (2005b) TEM study of a silicate-carbonate-microbe interface prepared by focused ion beam milling. Geochimica et Cosmochimica Acta, 69, 1413–1422.

Blum, A.E. (1994) Feldspars in weathering. In I. Parsons, Ed., Felsdspars and their reactions, p. 595–630. Kluwer, Dordrecht.

Brown, W.L. and Parsons, I. (1993) Storage and release of elastic strain energy: The driving force for low temperature reactivity and alteration of alkali feldspars. In J.N. Boland and J.D. Fitz Gerald, Eds., Defects and Processes in the Soild State: Geoscience Applications (The McLaren volume), p. 267–209. Elsevier, Amsterdam.

Donald, A.M. (2003) The use of environmental scanning electron microscopy for imaging wet and insulating materials. Nature Materials, 2, 511–516.

Eggleton, R.A. and Buseck, P.R. (1980) High resolution electron microscopy of feldspar weathering. Clays and Clay Minerals, 28, 173–178.

Fitz Gerald, J.D., Parsons, I., and Cayzer, N. (2006) Nanotunnels and pull-aparts: Defects of exsolution lamellae in alkali feldspars. American Mineralogist, 91, 772–783.

Heaney, P.J., Vicenzi, E.P., Giannuzzi, L.A., and Livi, K.J.T. (2001) Focused ion beam milling: A method of site-specific sample extraction for microanalysis of

Earth and planetary materials. American Mineralogist, 86, 1094–1099.
Hellmann, R., Penisson, J.M., Hervig, R.L., Thomassin, J.H., and Abrioux, M.F. (2003) An EFTEM/HRTEM high-resolution study of the near surface of labradorite feldspar altered at acid pH: evidence for interfacial dissolution-reprecipitation. Physics and Chemistry of Minerals, 30, 192–197.
Hochella, M.F. (2002) There's plenty of room at the bottom: Nanoscience in geochemistry. Geochimica et Cosmochimica Acta, 66, 735–743.
Hochella, M.F. and Banfield, J.F. (1995) Chemical weathering of silicates in nature: A microscopic perspective with theoretical considerations. In A.F. White and S.L. Brantley, Eds., Chemical weathering rates of silicate minerals, 31, 583 p. Reviews in Mineralogy, Mineralogical Society of America, Chantilly, Virginia.
Hodson, M.E., Lee, M.R., and Parsons, I. (1997) Origins of surface roughness of fresh and unweathered alkali feldspars. Geochimica et Cosmochimica Acta, 61, 3885–3896.
Kato, N.I. (2004) Reducing focused ion beam damage to transmission electron microscopy samples. Japanese Society of Microscopy, 53, 451–458.
Kawano, M. and Tomita, K. (2001) TEM-EDX study of weathered layers on the surface of volcanic glass, bytownite, and hypersthene in volcanic ash from Sakurajima volcano, Japan. American Mineralogist, 86, 284–292.
Lee, M.R. and Parsons, I. (1995) Microtextural controls of weathering of perthitic alkali feldspars. Geochimica et Cosmochimica Acta, 59, 4465–4488.
——— (1997) Compositional and microtextural zoning in alkali feldspars from the Shap granite and its geochemical implications. Journal of the Geological Society of London, 154, 183–188.
——— (1998) Microtextural controls on the diagenesis of detrital alkali feldspars: a case study of the Shap conglomerate (Lower Carboniferous), north-west England. Journal of Sedimentary Research, 68, 198–211.
Lee, M.R. and Smith, C.L. (2006) Scanning transmission electron microscopy using a SEM: applications to mineralogy and petrology. Mineralogical Magazine, 70, 561–572.
Lee, M.R., Waldron, K., and Parsons, I. (1995) Exsolution and alteration microtextures in alkali feldspar phenocrysts from the Shap granite. Mineralogical Magazine, 59, 63–78.
Lee, M.R., Hodson, M.E., and Parsons, I. (1998) The role of intragranular microtextures and microstructures in chemical and mechanical weathering: direct comparisons of experimentally and naturally weathered feldspars. Geochimica et Cosmochimca Acta, 62, 2771–2788.
Lee, M.R., Bland, P.A., and Graham, G. (2003) Preparation of TEM samples by focused ion beam (FIB) techniques: applications to the study of clays and phyllosilicates in meteorites. Mineralogical Magazine, 67, 581–592.
Liu, Y.L. and Jiao, C.G. (2005) Microstructure degradation of an anode/electrolyte interface in SOFC studied by transmission electron microscopy. Solid State Ionics, 176, 435–442.
Nugent, M.A., Brantley S.L., Pantano C.G., and Maurice, P.A. (1998) The influence of natural mineral coatings on feldspar weathering. Nature, 395, 588–591.
Obst, M., Gasser, P., Mavrocordatos, D., and Dittrich, M. (2005) TEM-specimen preparation of cell/mineral interfaces by Focused Ion Beam milling. American Mineralogist, 90, 1270–1277.
Parsons, I., Lee, M.R., and Smith, J.V. (1998) Biochemical evolution II: Origin of life in tubular microstructures on weathered feldspar surfaces. Proceedings of the National Academy of Sciences of the United States of America, 95, 15173–15176.
Parsons, I., Thompson, P., Lee, M.R., and Cayzer, N. (2005) Alkali feldspar microtextures as provenance indicators in siliciclastic rocks and their role in feldspar dissolution during transport and diagenesis. Journal of Sedimentary Research, 75, 921–942.
Petrović, R., Berner, R.A., and Goldhaber, M.B. (1976) Rate control in dissolution of alkali feldspars-I. Study of residual feldspar grains by X-ray photoelectron spectroscopy. Geochimica et Cosmochimca Acta, 40, 537–548.
Rubanov, S. and Munroe, P.R. (2003) The effect of gold sputter-coated films in minimizing damage in FIB-produced TEM specimens. Materials Letters, 57, 2238–2241.
——— (2004) FIB-induced damage in silicon. Journal of Microscopy, 214, 213–221.
Sheets, J.M. and Tettenhorst, R.T. (1997) Crystallographic controls on the alteration of microcline perthites from the Spruce Pine district, North Carolina. Clays and Clay Minerals, 45, 404–417.
Smith, C.L., Lee, M.R., and MacKenzie, M. (2006) New opportunities for nanomineralogy using FIB, STEM/EDX and TEM. Microscopy and Analysis, 111, 17–20.
Smith, J.V. (1998a) Atmospheric weathering and silica-coated feldspar: Analogy with zeolite molecular sieves, granite weathering, soil formation, ornamental slabs, and ceramics. Proceedings of the National Academy of Sciences of the United States of America, 95, 3366–3369.
——— (1998b) Biochemical evolution. I. Polymerization on internal, organophilic silica surfaces of dealuminated zeolites and feldspars. Proceedings of the National Academy of Sciences of the United States of America, 95, 3370–3375.
Smith, J.V. and Brown, W.L. (1988) Feldspar minerals (2nd edition), 1, 828 p. Springer Verlag, Berlin.
Smith, J.V., Arnold, F.P. Jr., Parsons, I., and Lee, M.R. (1999) Biochemical evolution: III. Polymerisation on organophilic silica-rich surfaces; crystal-chemical modeling; formation of first cells; geological clues. Proceedings of the National Academy of Sciences, 96, 3479–3485.
Stroud, R.M., Alexander, C.M.O., and MacPherson, G.J. (2000) A precise new method of microsampling chondritic material for transmission electron microscope analysis: preliminary application to calcium-aluminium-rich inclusions and associated matrix material in the Vigarano CV3 meteorite. Meteoritics and Planetary Sciences Supplement, 35, A153–154.
Takaoka, A. and Hasegawa, T. (2006) Observations of unstained biological specimens using a low-energy, high-resolution STEM. Journal of Electron Microscopy, 55, 157–163.
Tazaki, K. (1986) Observation of primitive clay precursors during microcline weathering. Contributions to Mineralogy and Petrology, 92, 86–88.
Waldron, K., Lee, M.R., and Parsons, I. (1994) The microstructures of perthitic alkali feldspars revealed by hydrofluoric acid etching. Contributions to Mineralogy and Petrology, 116, 360–64.
Wang, Z.G., Kato, T., Hirayama, T., Kato, N., Sasaki, K., and Saka, H. (2005) Surface damage induced by focused-ion-beam milling in a Si/Si p-n junction cross-sectional specimen. Applied Surface Science, 241, 80–86.
Wilson, M.J. and McHardy, W.J. (1980) Experimental etching of a microcline perthite and implications regarding natural weathering. Journal of Microscopy, 120, 291–302.
Wirth, R. (2004) Focused Ion Beam (FIB): A novel technology for advanced application of micro- and nanoanalysis in geosciences and applied mineralogy. European Journal of Mineralogy, 16, 863–876.
Xu, H. (1997) Surface characters of twin domains and exsolution lamellae in a feldspar crystal: Atomic force microscopy study. Materials Research Bulletin, 32, 1221–1227.
Xu, H., Veblen, D.R., Buseck, P., and Ramakrishna, B.L. (2000) TEM and SFM of exsolution and twinning in an alkali feldspar. American Mineralogist, 85, 509–514.
Zhu, C., Blue, A., and Veblen, D. (2004) Feldspar dissolution rates and clay precipitation in the Navajo aquifer at Black Mesa, Arizona, USA. In R.B. Wanty and R.R. Seal II, Eds., Water-Rock Interaction, p. 895–899. Taylor and Francis, London.
Ziegler, J.F. (2003) The stopping and range of ions in matter (SRIM-2003). Annapolis, Maryland, http://www.srim.org/SRIM/SRIM2003.htm.

Manuscript received September 18, 2006
Manuscript accepted March 11, 2007
Manuscript handled by Joshua Feinberg